

Lawrence Berkeley National Laboratory

LBL Publications

Title

Low-temperature processed bipolar metal oxide charge transporting layers for highly efficient perovskite solar cells

Permalink

<https://escholarship.org/uc/item/5wb8r1b7>

Authors

Singh, Mriganka
Yang, Rei-Ting
Weng, Da-Wei
[et al.](#)

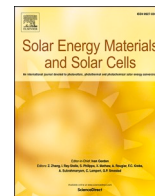
Publication Date

2021-03-01

DOI

10.1016/j.solmat.2020.110870

Peer reviewed



Low-temperature processed bipolar metal oxide charge transporting layers for highly efficient perovskite solar cells

Mriganka Singh^{a,b}, Rei-Ting Yang^{b,d}, Da-Wei Weng^{b,d}, Hanlin Hu^e, Anupriya Singh^b, Anisha Mohapatra^b, Yu-Ting Chen^b, Yu-Jung Lu^b, Tzung-Fang Guo^d, Gang Li^e, Hong-Cheu Lin^{a,f,*}, Chih Wei Chu^{b,c,*}

^a Department of Materials Science and Engineering, National Chiao Tung University, Hsinchu, Taiwan

^b Research Center for Applied Sciences, Academia Sinica, Taipei, Taiwan

^c College of Engineering, Chang Gung University, Guishan District, Taoyuan City, Taiwan

^d Department of Photonics, National Cheng Kung University, Tainan, Taiwan

^e Department of Electronic and Information Engineering, The Hong Kong Polytechnic University, Hung Hom, Kowloon, Hong Kong, China

^f Center for Emergent Functional Matter Science, National Chiao Tung University, Hsinchu, Taiwan

ARTICLE INFO

Keywords:

Low-temperature process
Nickel oxide
Cesium carbonate intercalation
Hole transporting layer
Electron transporting layer
Perovskite solar cells

ABSTRACT

Metal oxide charge carrier transporting materials have been incorporated in many ways in perovskite solar cells (PSCs) because of their excellent chemical stability, wide band gaps, and reasonable mobilities. Herein, we report a low-temperature solution-processed intercalation method for introducing metal oxides displaying bipolar transporting capability into PSCs. We intercalated p-type nickel oxide (NiO) with cesium carbonate (Cs₂CO₃) to function as hole and electron transport layers for inverted (p-i-n) and conventional planar (n-i-p) PSCs, respectively. When compared with the corresponding NiO-only hole transporting layer, the Cs₂CO₃-intercalated NiO layer displayed enhanced electron extraction without sacrificing its hole extraction capability. The power conversion efficiencies of the inverted and conventional planar PSCs reached as high as 12.08 and 13.98%, respectively. This approach not only realizes the bipolar extraction capacity of Cs₂CO₃-intercalated p-type metal oxides but also opens up a possible route for preparing interconnecting layers for tandem optoelectronics.

1. Introduction

The organic/inorganic hybrid (OIH) structures of perovskites having the formula ABX₃ (A = methylammonium, formamidinium, Cs; B = Pb, Sn, Sb; X = Cl, Br, I) can result in unique photovoltaic properties [1–4]. In particular, OIH-based perovskite solar cells (PSCs) have attracted a tremendous amount of attention as their efficiencies have increased dramatically from 3.8% in 2009 to over 25% in 2020 [5–7]. PSC structures fall into two categories: inverted (p-i-n) [1] and conventional planar (n-i-p) [8] frameworks. To date, the highest performance and longest device stability have arisen when using TiO₂ as the charge-carrier transporting layer (CTL) in planar PSCs [2,9]. Many charge-carrier transporting materials (CTMs) have been used to fabricate PSCs, including organic charge-carrier transporting materials [OCTMs; e.g., poly(3,4-ethylenedioxythiophene):poly(styrenesulfonic acid) (PEDOT:PSS) [10,11], poly[bis(4-phenyl)(2,4,6-trimethylphenyl

amine] (PTAA) [12], poly(3-hexylthiophene-2,5-diyl) (P3HT) [13], 2,2',7,7'-tetrakis(*N,N*-di-*p*-methoxyphenylamino)-9,9'-spirobifluorene (spiro-OMeTAD) [6,6,14], -phenyl C₆₁ butyric acid methyl ester (PCBM) [15], C₆₀ [11] and inorganic charge-carrier transporting materials (ICTMs; e.g., TiO₂ [9], SnO₂ [16], NiO [17], ZnO [18], Cu₂O [19], CuSCN [20], CuI [21,22], CdS [23], Cu₂BaSnS₄ [24]). A drawback to having an organic component in a lead perovskite is that it might readily degrade when exposed to moisture and the atmosphere, due to the low formation energy [25]. In addition, OCTMs can suffer from a light-soaking problem, due to the dominant accumulation of photoexcited carriers in their devices, resulting in instability [26–28]. CTLs play critical roles in sandwiching the perovskite absorber layer and helping to enhance the device stability of PSCs. Metal-oxide charge-carrier transporting materials (MCTMs) have been the best replacements for OCTMs in optoelectronic applications because of their inexpensive preparation, high device efficiencies, long-term device stability, high mobilities, and

* Corresponding author. Research Center for Applied Sciences, Academia Sinica, Taipei, Taiwan.

** Corresponding author. Department of Materials Science and Engineering, National Chiao Tung University, Hsinchu, Taiwan.

E-mail addresses: linhc@cc.nctu.edu.tw (H.-C. Lin), gchu@gate.sinica.edu.tw (C.W. Chu).

wide band gaps [16,29]. Furthermore, MCTMs can be even more beneficial for optoelectronic applications when the metal oxide displays bipolar charge-carrier (both hole and electron) extraction capabilities upon interaction with another metal [30,31].

Li et al. used a high-temperature intercalating method to demonstrate continuous changes in the work function, spanning 1.1 eV, for V_2O_5 and MoO_3 through intercalation of Cs in bulk heterojunction (BHJ) optoelectronic devices [30]. Later, the same group reported a Cs-intercalated metal oxide for bipolar charge-carrier extraction in BHJ optoelectronic devices having the same structure [31]. Irwin et al. used nickel oxide (NiO) as a replacement for organic HTM interfacial layers in BHJ solar cells [32]. The layered crystal structures of metal oxides are held together by van der Waals forces, readily allowing the intercalation of other metal cations or atoms inside the metal oxide [30,33]. Doping of Cs has led to the preparation of solution-processed metal oxides for use as either electron transporting layers (ETLs; e.g., TiO_2 [34], ZnO [35], AZO [36]) or hole transporting layers (HTLs; e.g., NiO_x [37], V_2O_5 [38]) [39]. Furthermore, other metals have been explored for their the carrier blocking effects, as well as their abilities to enhance optical and electrical properties [40,41]. All of these doping methods have required the metal oxide transport layers to be sintered at high temperatures (>400 °C), thereby resulting in high energy consumption. Favorable energy level alignment with the active layer has been reported recently when using Cs [42], as dopants for NiO to function as a perfect HTM [37, 43,44]. Moreover, NiO_x is one of the most suitable HTLs for PSCs because of its wide band gap energy (3.4–4.0 eV), high chemical stability, and good optical transparency and conductivity [29,45,46]. NiO is, however, quite difficult to produce at low-temperature for use as a HTM. Chen et al. found that the doping of Cs (at high temperature) in Cs: NiO_x improved its charge extraction capabilities and resulted in the power conversion efficiency (PCE) reaching 19.35% [37]. Low-temperature intercalation of metal oxides has not, however, been realized previously in the fabrication of PSCs. We are the first group to demonstrate the technique of preparing ground NiO nanoparticles and intercalation Cs_2CO_3 in NiO at low temperature, which is a straightforward and eco-friendly physical method. Moreover, comparing to existing reports on pristine NiO HTL and doping NiO HTL, the new bipolar transporting layer is very unique that it is chemically pure and without ligand.

In this paper, we report a high-energy wet-milling grinding method to prepare the NiO NPs at a room temperature and a low-temperature solution-processing method for the intercalation of cesium carbonate (Cs_2CO_3) into NiO, resulting in bipolar charge-carrier (both hole and electron) extraction capability for inverted (p–i–n) and conventional planar (n–i–p) PSCs. The resulting device structures, both inverted and planar PSCs, displayed their highest PCEs of 12.08 and 13.98%, respectively. In comparison with the corresponding device featuring an HTL of NiO alone, the Cs_2CO_3 -intercalated NiO layer exhibited enhanced electron extraction without sacrificing its hole extraction capability. This new material for bipolar charge-carrier extraction has the potential to serve as an inexpensive, scalable, environmentally stable, and low-energy-consumption interconnection layer for emerging flexible tandem photovoltaic devices.

2. Experimental section

2.1. Materials

Nickel oxide (NiO) nano powder (product no 28N-0801) was purchased from Infrant® Advanced Materials (USA). Zirconium dioxide (ZrO_2 , zirconia) beads (density: 5.95 g cm^{-3} ; size: 50 μm) were obtained from Oriental Cera TEC (Taiwan). Cs_2CO_3 (99.995% metal basis) was obtained from Aldrich (USA). Lead(II) iodide (PbI_2 , 99.998%) and 4-*tert*-butylpyridine (t-BP) were purchased from Alfa-Aesar. Methylammonium iodide (MAI) was obtained from Greatcell Solar (Australia). Bis(trifluoromethane)sulfonimide lithium salt (Li-TFSI) was purchased

from UR Company (Taiwan). spiro-OMeTAD, poly(methyl methacrylate) (PMMA), and $PC_{60}BM$ were obtained from Luminescence Technology (Taiwan). Isopropyl alcohol (IPA), ethanol, 2-methoxyethane, dimethylformamide (DMF), dimethyl sulfoxide (DMSO), acetonitrile (ACN), methylbenzene (toluene), and chlorobenzene (CB) were purchased from Sigma–Aldrich (USA). All chemicals and solvents were used directly without purification.

2.2. Hole and electron transporting layers

- (1) Ground NiO NPs: The NiO NPs were prepared through a new high-energy wet-milling grinding method, using procedures similar to those reported previously for tin oxide and titanium oxide materials [8,16]. The NiO powder (3 wt%) in IPA was ground together with zirconia beads (ca. 500 g) under ambient conditions at 2000 rpm. A schematic representation of the grinder, dispersing machine (AG-1000, Allgen Technology), and electric stirrer is provided in the Supporting Information (SI, Fig. S1a). After 8 h, the NiO NPs were separated (the high-density zirconia beads settled at the bottom). A sol–gel NiO_x was prepared by mixing 0.5 M nickel formate dihydrate in ethylene glycol, based on literature procedures [47,48].
- (2) Cs_2CO_3 -Intercalated NiO (NiO + Cs_2CO_3): To prepare the NiO + Cs_2CO_3 precursor solution, Cs_2CO_3 (50 mg) was dissolved in 2-methoxy methane/ethanol (1:1, v/v; 1 mL; used as stock solution) and then various doping concentrations (1–10%) of the Cs_2CO_3 solution (from prepared 1 mL) were added into the ground NiO solution (0.5 wt%; diluted in IPA).

2.3. Precursor solution of perovskite, $PC_{60}BM$, spiro-OMeTAD, and PMMA

A perovskite precursor solution of PbI_2 (1 M) and MAI (1 M) in anhydrous DMF/DMSO (6:4, v/v) was heated at 65 °C overnight. A solution of $PC_{60}BM$ (20 mg) in CB (1 mL) and spiro-OMeTAD (80 mg) in CB (953 μL) was doped with Li-TFSI [520 mg in ACN (1 mL); 18 μL] and t-BP (29 μL). The solution of PMMA (0.6 mg) in CB/toluene (9:1, v/v; 1 mL) was prepared as reported previously [49].

2.4. Device fabrication

Indium tin oxide (ITO) substrates ($<10\ \Omega\ \text{cm}^{-1}$) were patterned by etching with a standard solution of concentrated HCl, washing with deionized water and detergent, sonicating in IPA and acetone (40 min each), blowing dry under N_2 , and storing in an oven overnight. The cleaned ITO substrates were treated with UV ozone for 30 min to eliminate any contamination. To deposit NiO (ca. 40 nm) on the UV-treated substrate, the 0.5 wt% dispersion of NiO in IPA was sonicated for at least 30 min prior to use. The NiO and NiO + Cs_2CO_3 layers were deposited by spin-coating (3000 rpm, 30 s) and then subjected to low temperature annealing (150 °C, 30 min). The NiO_x layer was deposited on the ITO substrate at 3000 rpm for 30 s, followed by high temperature annealing (400 °C, 10 min). The perovskite layer was deposited using a one-step anti-solvent method. The perovskite (ca. 400 nm) precursor was spin-coated (first at 2500 rpm for 15 s; then at 5000 rpm for 10 s) on the HTL/ETL; during the second spin-coating process, a droplet of CB (250 μL) was placed on the perovskite, which was then annealed at 100 °C for 10 min. A thick $PC_{60}BM$ layer (ca. 300 nm) was deposited by solution-processing (1500 rpm, 40 s) on the perovskite-coated sample, which was then annealed at 100 °C for 10 min spiro-OMeTAD (ca. 270 nm) was deposited on the perovskite film through spin-coating (3000 rpm, 30 s). A thin passivation or protection layer of PMMA (ca. 10 nm) was deposited by spin-coating (6500 rpm, 30 s) on the perovskite sample and then annealing (100 °C, 1 h). The top metal oxide (NiO) HTL layer deposited through solution-processing (3000 rpm, 30 s) was annealed at low temperature (100 °C, 30 min). C_{60} (ca. 30 nm) and BCP (ca. 10 nm)

layers were formed through thermal deposition. Finally, aluminum (Al) and silver (Ag) electrodes (ca. 100 nm) were deposited through thermal evaporation at 1×10^{-6} torr. The active area of the device was 0.1 cm^2 . The first layer, either the NiO HTL or NiO + Cs_2CO_3 ETL, was deposited under ambient conditions; the other active layers and other ETLs/HTLs were processed under a N_2 atmosphere.

2.5. Device characterization

Ultraviolet photoelectron spectroscopy (UPS; PHI 5000 Versa Probe) was performed using an Al $K\alpha$ X-ray source (1486.6 eV) to measure the Fermi edge and valance band shift of the NiO NPs and the Cs_2CO_3 -intercalated NiO, using the He(I) (source: UV light) emission (21.22 eV, ca. 50 W). Transmission electron microscopy (TEM) images of the NiO NPs were recorded using a JEOL JEM-2100F instrument. Crystal structures were recorded using X-ray diffraction (XRD; Bruker AXS, D8 Advance) and Cu $K\alpha$ radiation, under operating conditions of 40 kV and 40 mA. X-ray photoelectron spectroscopy (XPS; PHI 5000 Versa Probe) with an Al $K\alpha$ X-ray source (1486.6 eV) was used to measure the oxidation state. Surface morphologies were imaged using atomic force microscopy (AFM; Bruker Dimension Icon atomic force microscope) and scanning electron microscopy (SEM; FEI Nova 200 microscope, 15 kV). Surface potential (KPFM) was imaged using Asylum Research. Transmission and absorption (Tauc plot) spectra were recorded using a Jacobs V-670 UV-Vis spectrophotometer. The J - V characteristics of the devices were measured using a solar simulator (Thermal Oriol) and a Xe lamp, giving a simulated AM 1.5 spectrum (100 mW cm^{-2}); prior to device measurement (inside a glove box), the light intensity was calibrated using a mono-silicon photodiode with a KG-5 color filter (Hamamatsu). The encapsulated device was used to measure external quantum efficiency (EQE; Enli Tech, Taiwan) spectra. The J - V curves were measured in both reverse (from +1.2 to -0.2 V) and forward (from -0.2 to +1.2 V) voltage sweeps without any delay time (0 ms). Steady state PL spectra (Attody 800, Attocube) were recorded at room temperature. The

wavelength of the excitation source was 405 nm. The perovskite samples were pumped by a Ti:sapphire laser (Spectra Physics, 800 nm, 100 fs, 80 MHz) prior to measurement. A 100x objective lens (0.82 NA; Attocube) for photoluminescence (PL) was used to focus the laser to a tiny spot (diameter: $1 \mu\text{m}$) with an average power density of 53 kW cm^{-2} . Electrochemical impedance spectroscopy (EIS) was performed using an SI 1296 dielectric interface (Solartron) and an SI 1260 impedance/gain-phase analyzer in the dark (bias: 0.8 V). Grazing-incidence wide-angle X-ray scattering (GIWAXS) were performed at the 23A beamline of the National Synchrotron Radiation Research Center (NSRRC), Hsinchu, Taiwan [50].

3. Results and discussion

Fig. 1a presents a bright-field TEM image of the ground NiO NPs. Fig. S1a (SI) displays a schematic representation of the procedure used to prepare the ground NiO NPs using a ball-miller (grinder); details are provided in the Experimental section. Real-time photographs of the non-ground NiO and ground NiO NPs are provided in Figs. S1b and S1c (SI), respectively. Fig. S2 (SI) presents a bright-field TEM image of the non-ground NiO, revealing large clumps and aggregation. The high-resolution TEM (HRTEM) image of the ground NiO NPs (Fig. 1b) suggested crystal lattice d -spacings of 0.241 and 0.208 nm, corresponding to interplanar distances in the (111) and (200) directions, respectively. The selective area diffraction pattern of the ground NiO NPs (Fig. 1c) revealed numerous ring (111), (200), and (220) orientations, suggesting a lower degree of crystallinity. The dimensions of the NiO NPs, calculated from 36 individual particles in Fig. 1a, revealed (Fig. 1d) a measured average particle size of approximately 9 nm ($8.39 \pm 1.99 \text{ nm}$). Fig. S3a (SI) and Fig. S3b (SI) presents a bright-field TEM image and HRTEM, respectively, of the intercalated Cs_2CO_3 in NiO film, revealing the bigger particle size ($>10 \text{ nm}$) compared with ground NiO NPs due to aggregation of NiO and Cs_2CO_3 . Moreover, TEM studies are widely used to analysis the nanoscale diffusion, interface quality and elemental

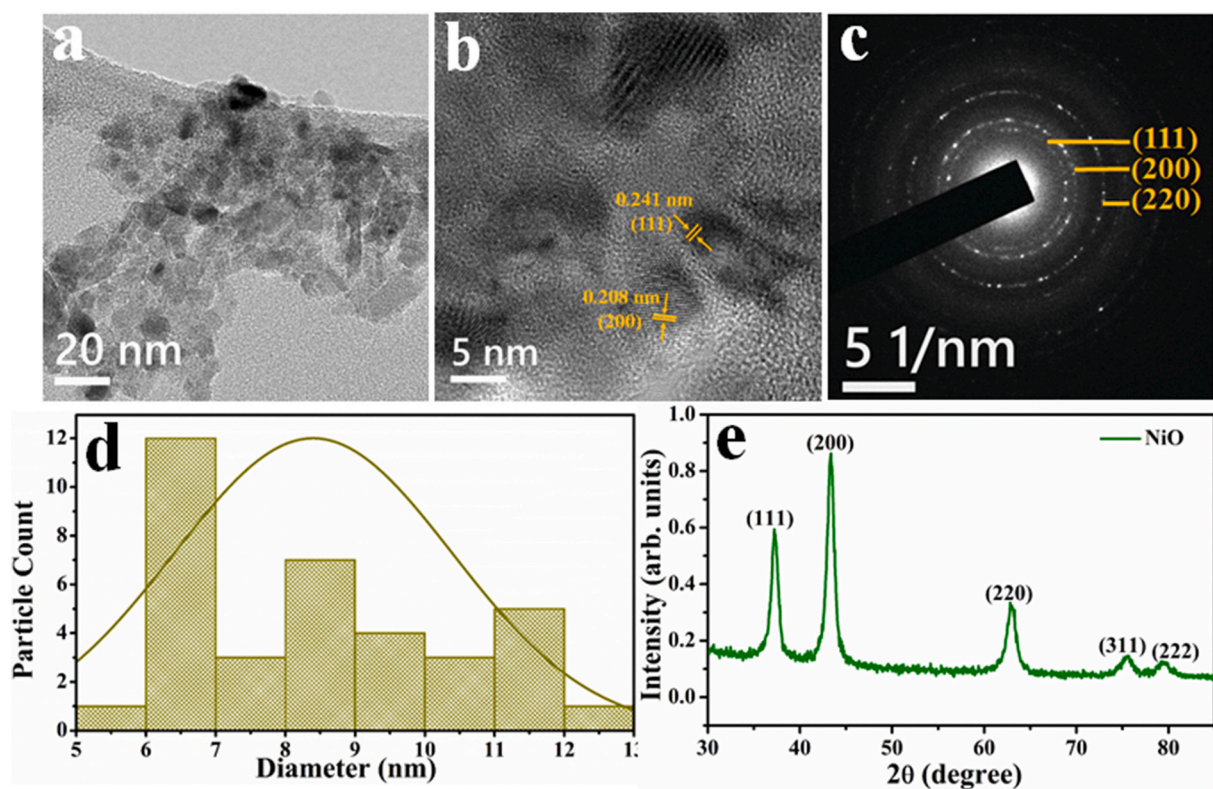


Fig. 1. (a) Bright-field TEM image, (b) HRTEM image, and (c) selective-area diffraction pattern of the ground NiO NPs. (d) Particle count plot calculated (36 individual particles) from (a), giving an average NiO NP particle size of approximately 9 nm ($8.39 \pm 1.99 \text{ nm}$). (e) XRD pattern of a thin film of the ground NiO NPs.

composition [51,52]. Fig. S3c (SI) and Fig. S3d (SI) presents a HRTEM of pristine NiO and intercalated Cs_2CO_3 in NiO on perovskite, respectively. Fig. 1e presents a XRD pattern of the ground NiO NPs, featuring the same set of diffraction peaks of the (111), (200), (220), (311), and (222) crystals planes, consistent with literature values (JCPDS 78-0423) [53]. The higher intensities of the signals in this XRD pattern suggested complete degradation of the large clumps of non-ground NiO into smaller particles; the absence of any extra peaks suggested that the ground NiO NPs were of high purity [53]. Fig. S4 (SI) displays the transmission spectra of the NiO NPs and the 5% Cs_2CO_3 -intercalated NiO (NiO + 5% Cs_2CO_3) films on quartz substrates. Both films exhibited good transmissions in the range 300–800 nm, but the transmission of the NiO + 5% Cs_2CO_3 film was slightly poorer in the range 300–500 nm. The inset to Fig. S4 (SI) presents real-time photographs of the ground NiO NPs and the NiO + Cs_2CO_3 blend in solution and in the form of films.

The compositions and electronic structures of the NiO_x (prepared using a sol-gel method; see Experimental section), the ground NiO NPs, and the Cs_2CO_3 -intercalated NiO were confirmed using XPS (Fig. 2). The Ni $2p_{3/2}$ and O 1s XPS spectra of the NiO_x -based film revealed the presence of Ni^{3+} and Ni^{2+} states in a non-stoichiometric manner. The Ni $2p_{3/2}$ and O 1s signals appeared (Fig. 2a) at 855.4 eV (Ni^{3+}), 853.6 eV (Ni^{2+}), 531.9 eV (Ni^{3+}), and 530.1 eV (Ni^{2+}) [17]. The ground NiO NPs and the Cs_2CO_3 -doped films were stoichiometric, with peaks appearing only for the Ni^{2+} state (Fig. 2b–d). The XPS spectra of the undoped and Cs_2CO_3 -doped films of NiO featured Ni $2p_{3/2}$ peaks at 854.8 and 854.8 eV and O 1s peaks at 531.8 and 532.0 eV. No Cs 3d peaks were observed in the case of the NiO NPs sample, but the Cs_2CO_3 -intercalated NiO film provided signals at 740.2 (Cs $3d_{3/2}$) and 725.8 (Cs $3d_{5/2}$) eV [54].

Figs. 3a–c present the device architectures of three kinds of NiO-based PSC frameworks. The first device framework is an inverted structure (device A) featuring ITO glass, NiO + Cs_2CO_3 as the HTL, methylammonium lead triiodide ($\text{CH}_3\text{NH}_3\text{PbI}_3$) as the active layer, PC_{60}BM as the ETL, and $\text{C}_{60}/\text{BCP}/\text{Al}$ as the electrode. The second device framework is a conventional planar structure (device B) featuring ITO glass, NiO + Cs_2CO_3 as the ETL, $\text{CH}_3\text{NH}_3\text{PbI}_3$ as the active layer, spiro-OMeTAD as the HTL, and MoO_3/Ag as the electrode. The third device framework has metal oxide functioning as both the ETL and HTL within a single PSC system (device C); it features ITO glass, NiO + Cs_2CO_3 as the ETL, $\text{CH}_3\text{NH}_3\text{PbI}_3$ as the active layer, PMMA for surface passivation, NiO as the HTL, and Ag as the electrode. The current density–voltage (J – V) curves of devices A, B, and C were measured in both forward and reverse voltage scans (Fig. 3d–f, respectively); the device performance data is

summarized in Table 1. Another inverted device architecture for the NiO NP-based PSC (device D: glass/ITO/NiO/ $\text{CH}_3\text{NH}_3\text{PbI}_3$ / $\text{PC}_{60}\text{BM}/\text{C}_{60}/\text{BCP}/\text{Al}$) is displayed in Figs. S5a–b (SI). Furthermore, to gain more insight into the effect of a PSCs featuring a single layer of Cs_2CO_3 and NiO NPs (n–i–p structure), device E (glass/ITO/ Cs_2CO_3 / $\text{CH}_3\text{NH}_3\text{PbI}_3$ /spiro-OMeTAD/ MoO_3/Ag) and device F (glass/ITO/NiO/ $\text{CH}_3\text{NH}_3\text{PbI}_3$ /spiro-OMeTAD/ MoO_3/Ag) were also prepared (Figs. S5c–d SI); their device performance data are summarized in Table S1 (SI). The J – V curves of devices A and device B (Figs S6 and S7, SI) were recorded to determine the effect of doping various concentrations of Cs_2CO_3 in the NiO NPs used as the HTLs and ETLs; the data are summarized in Tables S2 and S3 (SI), respectively. Doping concentrations of 0, 1, 2.5, 5, and 10% of Cs_2CO_3 into the NiO-based inverted (p-type) and conventional planar (n-type) device structures resulted in PCEs of 13.27, 12.29, 12.25, 12.08 and 10.24%, respectively, and 4.02, 10.62, 13.82, 13.98, and 12.93%, respectively (Fig. 4). In case of the inverted device structure, the PCE decreased continually upon increasing the doping concentration of Cs_2CO_3 . In contrast, for the planar device structure, the PCE increased upon increasing the doping concentration of Cs_2CO_3 up to 5%, but decreased thereafter. Thus, we chose NiO + 5% Cs_2CO_3 to be the optimized material for use as an HTL in device A and as an ETL in device B. The J – V curves of the PSCs incorporating the Cs_2CO_3 -intercalated NiO as the HTL (in device A) and ETL (in device B), recorded to determine the optimized thicknesses (30, 40, or 50 nm), are presented in Figs. S8 and S9 (SI), respectively; the device performance data are summarized in Tables S4 and S5 (SI), respectively. The optimized thickness was 40 nm for both devices A and B, fabricated by a blending 5% Cs_2CO_3 and 0.5 wt % of the NiO NP solution. The champion performances of devices A, B, and C were obtained in the reverse scan direction: open circuit voltages (V_{oc}) of 0.95, 1.09, and 0.86 V, respectively; current densities (J_{sc}) of 22.01, 20.32, and 19.36 mA cm^{-2} , respectively; fill factors (FFs) of 57.79, 63.15, and 58.56%, respectively; and PCEs of 12.08, 13.98, and 9.75%, respectively. The champion performances of devices A, B, and C were obtained in the forward scan direction: open circuit voltages (V_{oc}) of 0.94, 1.09, and 0.85 V, respectively; current densities (J_{sc}) of 22.17, 20.30, and 19.78 mA cm^{-2} , respectively; fill factors (FFs) of 57.84, 62.43, and 49.72%, respectively; and PCEs of 12.05, 13.83, and 8.36%, respectively. The discrepancy of FF in device C derived from both reverse and forward scans direction is about 10%, revealing that huge hysteresis problem compare with device A, and device B. The higher FF, and V_{oc} of device B leads to high efficiency compare to device A and device C, revealing the better energy level alignment with active layer in

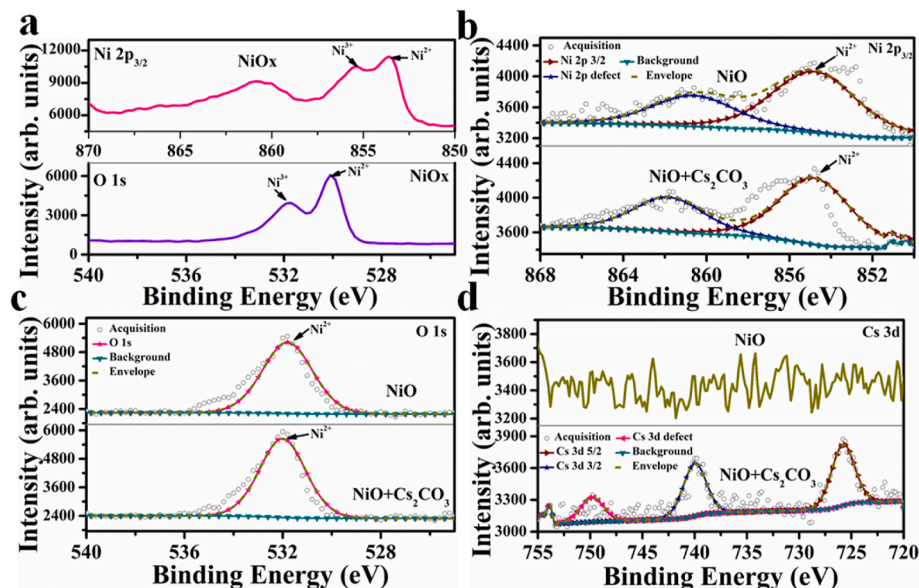


Fig. 2. (a) Ni $2p_{3/2}$ and O 1s XPS spectra of NiO_x ; (b–d) XPS spectra of NiO and NiO + Cs_2CO_3 ; (b) Ni $2p_{3/2}$, (c) O 1s, and (d) Cs 3d spectra.

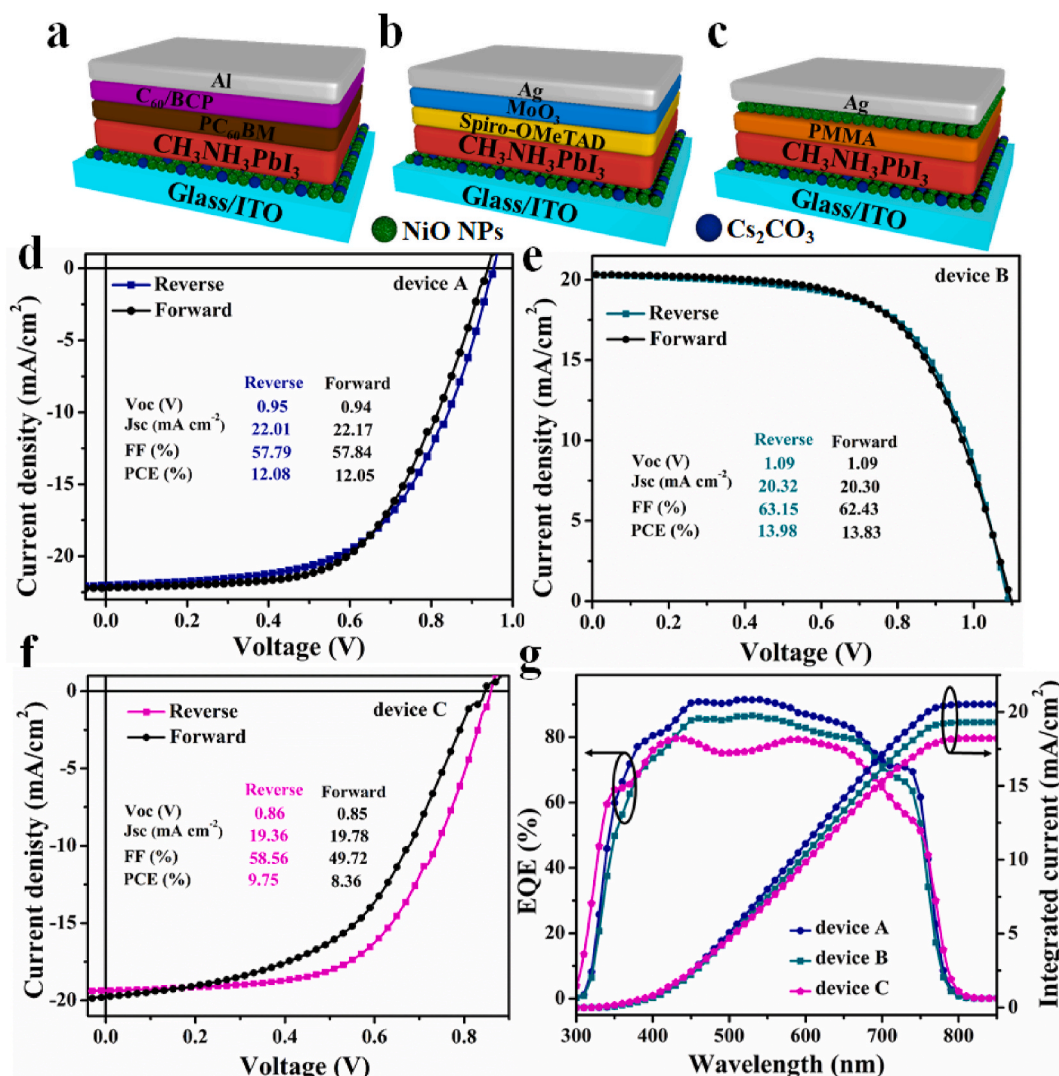


Fig. 3. (a–c) Schematic representations of the structures of the PSC devices (a) A, (b) B, and (c) C. (d–f) J - V curves (forward and reverse biases) of the highest performing of the various PSC devices (d) A, (e) B, and (f) C. (g) EQE spectra of the PSC devices A–C.

Table 1

Photovoltaic parameters of PSCs incorporating different structures performed under a simulated AM 1.5G solar illumination (100 mW cm⁻²).

Device	PSC structure	V_{oc} (V)	J_{sc} (mA cm ⁻²)	FF (%)	PCE (%)
A	glass/ITO/NiO	0.95	22.01	57.79	12.08
	+ Cs_2CO_3 /	0.94 ±	21.43 ±	58.02 ±	11.72 ±
	$\text{CH}_3\text{NH}_3\text{PbI}_3$ / $\text{PC}_{60}\text{BM}/\text{C}_{60}/$ BCP/Al	0.01	0.80	1.67	0.52
B	glass/ITO/NiO	1.09	20.32	63.15	13.98
	+ Cs_2CO_3 /	1.04 ±	20.45 ±	58.50 ±	12.43 ±
	$\text{CH}_3\text{NH}_3\text{PbI}_3$ / spiro-OMeTAD/ MoO_3/Ag	0.02	1.09	3.13	0.78
C	glass/ITO/NiO	0.86	19.36	58.56	9.75
	+ Cs_2CO_3 /	0.86 ±	19.17 ±	50.23 ±	8.28 ±
	$\text{CH}_3\text{NH}_3\text{PbI}_3$ / PMMA/NiO/Ag	0.01	1.21	6.95	1.26

*Averages ± standard deviations (SD) calculated from 12 individual cells.

planar structure than inverted structure. In addition, devices D, E, and F provided values of V_{oc} of 0.95, 0.83, and 0.60 V, respectively; values of J_{sc} of 22.21, 17.98, and 19.61 mA cm⁻², respectively; FFs of 62.87,

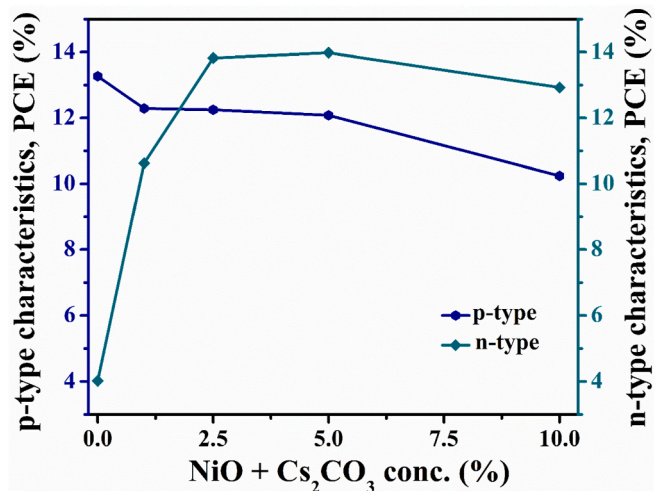


Fig. 4. PCEs plotted with respect to the doping concentration of intercalated Cs_2CO_3 in NiO-based p-type (device A) and n-type (device B) structures.

50.70, and 34.18%, respectively; and PCEs of 13.27, 7.57, and 4.02%, respectively. The external quantum efficiency (EQE) spectra and integrated photo-current densities of the champion PSCs of various device configurations A, B, and C are displayed in Fig. 3g. Similar absorption range was visible to near IR region (ca. 300–800 nm) obtained for various device configuration with peak EQEs of approximately 92, 85, and 80% of device A, device B, and device C, respectively. The integrated current densities of devices A, B, and C calculated from these EQE curves were 20.52, 19.30, and 18.22 mA cm⁻², respectively, which is close to (device A = 22.01, device B = 20.32, and device C = 19.36 mA cm⁻²) measured from *J-V* curves. The discrepancy in current density derived from EQE and measured from *J-V* curves about less than 7% [52]. To determine the reproducibility of these devices, Fig. 5a and b displays the measured performance data of 12 individual PSC cells for each type of structure. The statistical data of devices A, B, and C in the reverse scan direction provided values of V_{oc} of 0.94 ± 0.01 , 1.04 ± 0.02 , and 0.86 ± 0.01 V, respectively; values of J_{sc} of 21.43 ± 0.80 , 20.45 ± 1.09 , and 19.17 ± 1.21 mA cm⁻², respectively; FFs of 58.02 ± 1.67 , 58.50 ± 3.13 , and $50.23 \pm 6.95\%$, respectively; and PCEs of 11.72 ± 0.52 , 12.43 ± 0.78 , and $8.28 \pm 1.26\%$, respectively. To examine the chemical stability of the physically prepared ground NiO NPs, stability tests for inverted PSCs incorporating the NiO NPs (device D) were

performed under an inert atmosphere (Fig. 5 c-f) on four individual cells. Device D exhibited good stability for up to 50 days, losing only 25% of its initial PCE.

The band alignment of the electrode interlayers and active layer is a significant characteristic for defining the p-i-n and n-i-p device architectures of PSCs [16,37]. UPS [He(I)] spectra were recorded to measure the Fermi levels and valance bands (VBs) of the Cs₂CO₃-intercalated NiO samples prepared at various doping concentrations, using equation ($\phi = h\nu - (E_f - E_i)$; where $h\nu = 21.2$ eV) [55]. The full UPS spectra are presented in Fig. 6a. The Fermi levels [work functions] after doping various amounts (0–10%) of Cs₂CO₃ into NiO were 4.02 [5.18] (0%), 3.85 [5.02] (1%), 3.71 [4.94] (2.5%), 4.38 [3.89] (5%), and 4.10 [3.10] (10%) eV, respectively, as calculated from Fig. 6b and c. Remarkably, the Fermi edge shift could increase continually to as high as 1.81 eV for the 5% Cs₂CO₃-intercalated NiO sample, as displayed in Fig. 6a (blue spectra). This Fermi edge shift allowed the NiO sample to change the nature of its semiconductor characteristic from p-to n-type. The band gap energies (E_g) measured from Tauc plots (Fig. 6d) for the 0, 1, 2.5, 5, and 10% Cs₂CO₃-intercalated NiO samples were 3.69, 3.68, 3.61, 3.46, and 3.57 eV, respectively. By varying the amount (0–10%) of Cs₂CO₃ doped into the metal oxide, continuous modification of the work function of the Cs₂CO₃-intercalated NiO as possible, as indicated in the

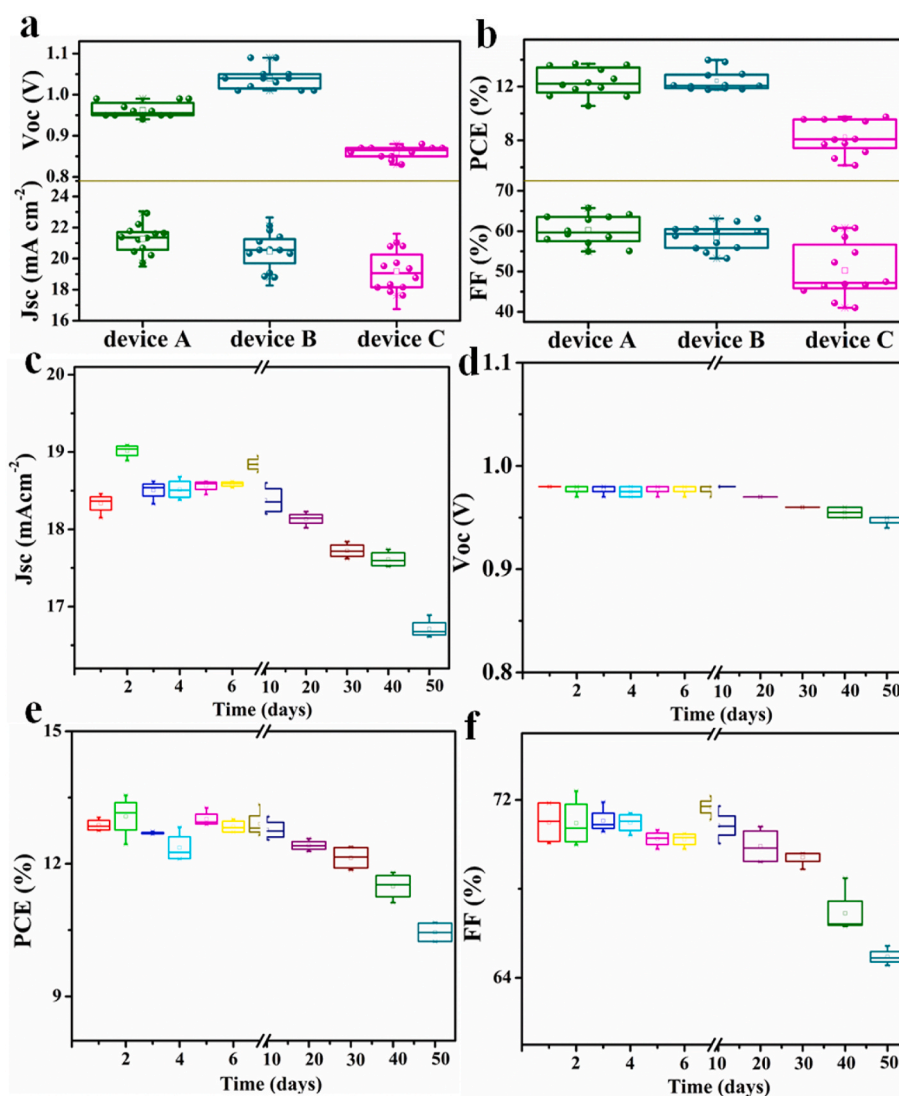


Fig. 5. (a, b) Box charts of the performance data of PSC devices A–C, calculated in the reverse scan direction only, determined from 12 individual cells: (a) J_{sc} (mA cm⁻²) and V_{oc} (V); (b) FF (%) and PCE (%). Box charts of the device stability of the PSC incorporating NiO NPs as the HTL (device D), stored in a glove box without encapsulation: (c) J_{sc} (mA cm⁻²), (d) V_{oc} (V), (e) PCE (%), and (f) FF (%).

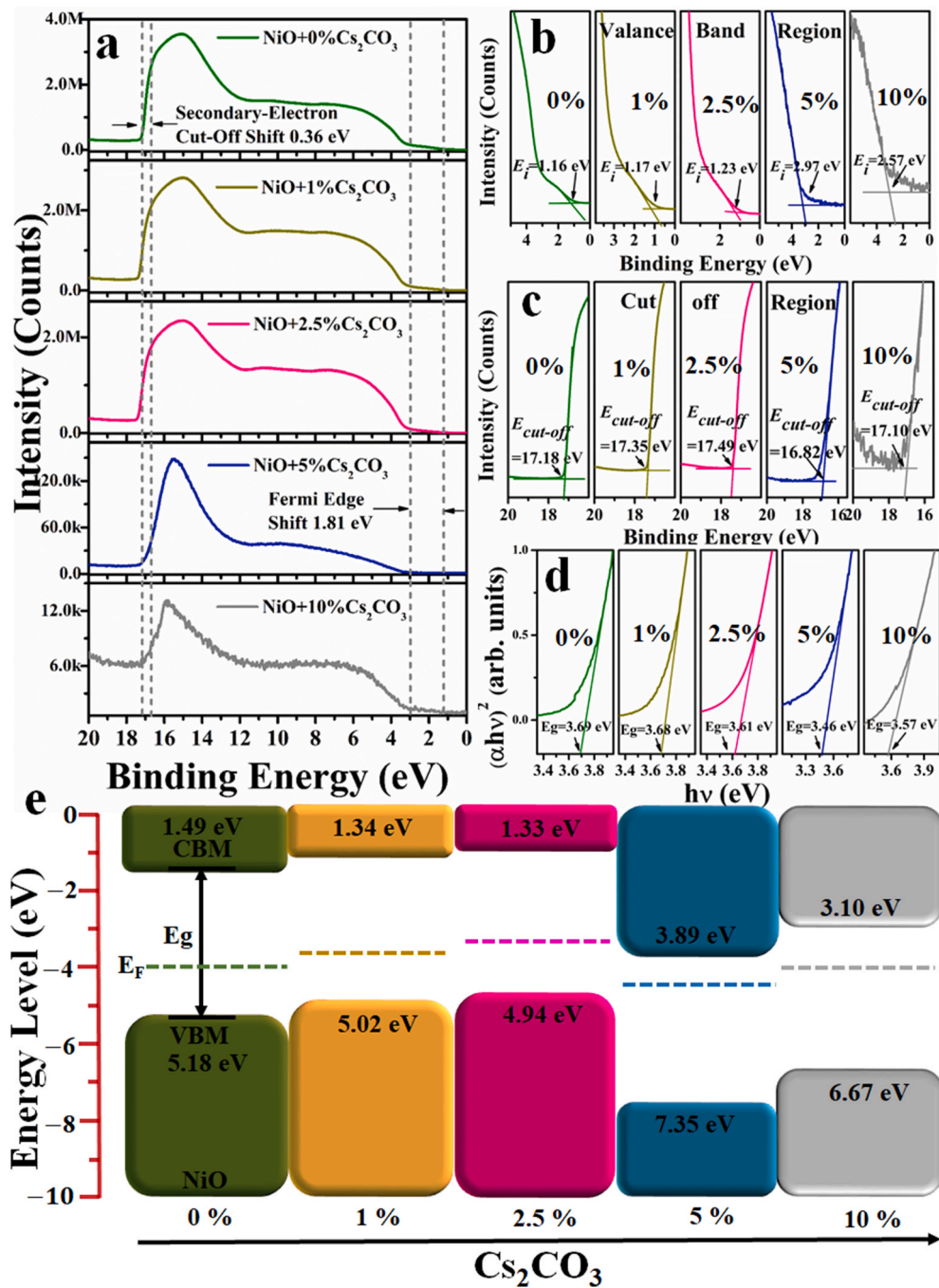


Fig. 6. (a–d) UPS [He(I)] spectra of NiO intercalated with Cs₂CO₃ at doping concentrations of 0, 1, 2.5, 5, and 10%: (a) full UPS spectra; (b) onset energy spectra; (c) cut-off energy spectra; (d) energy band gap data from Tauc plots. (e) Energy band diagram of NiO intercalated with Cs₂CO₃ at doping concentrations of 0, 1, 2.5, 5, and 10%.

energy band diagram in Fig. 6e. Nevertheless, a large amount of the Cs₂CO₃ dopant in the metal oxide would introduce interfacial trap states and increase the defect density, thereby decreasing the device performance [37]. The 5% Cs₂CO₃-intercalated NiO was the optimized sample. In general, the lowest unoccupied molecular orbitals (LUMOs) of ETLs have band gaps of 4.05–3.99 eV for TiO₂ [8] and 3.82 eV for Cs₂CO₃ [56], with a value of 3.9 eV for a CH₃NH₃PbI₃ active layer [57]. For the 5% Cs₂CO₃-intercalated NiO sample, the work function (3.89 eV) was similar to the LUMO energy level of the active layer, thereby providing better band alignment between the two layers. The results obtained from UPS in Fig. 6e, doping concentration of 1% and 2.5% shows roughly p-type behavior; 5% and 10% shows roughly n-type behavior. Fig. S10

(SI) displays the surface potentials maps (KPFM) and surface line profiles of the various doping Cs₂CO₃ concentration in NiO films. Low surface potentials are found for 1% Cs₂CO₃ doping and higher potentials are found for 2.5% which is agree with the Fermi levels (E_F); closer to VBs and towards to conduction bands (CBs), respectively. High surface potentials are found for 5% Cs₂CO₃ doping and lower potentials are found for 10% which is agree with the E_F ; closer to CBs and towards to VBs, respectively [58].

Figs. S11a–c (SI) presents cross-sectional SEM images of devices having structures similar to those of devices A, B, and C in Fig. 3a–c, respectively. Top-view SEM and AFM images of the NiO NPs and Cs₂CO₃-intercalated NiO on glass/ITO substrates are displayed in

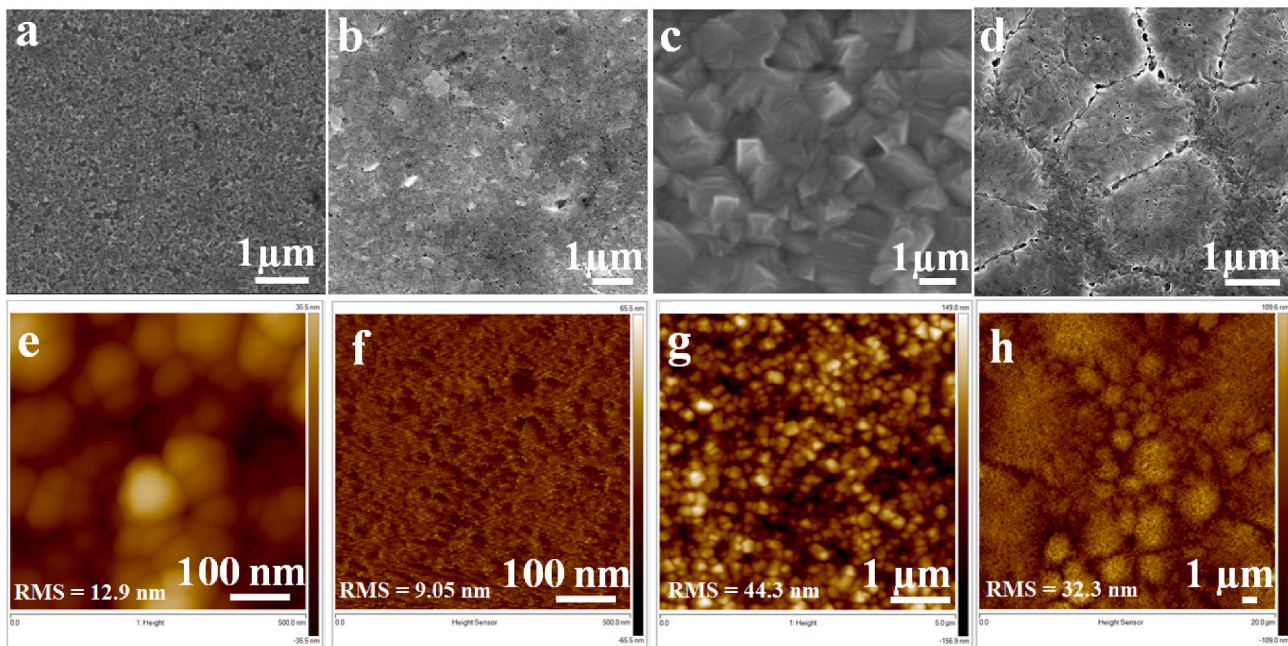


Fig. 7. (a–d) SEM and (e–h) AFM images of (a, e) NiO, (b, f) NiO + Cs₂CO₃, (c, g) NiO/CH₃NH₃PbI₃, and (d, h) NiO + Cs₂CO₃/CH₃NH₃PbI₃ on glass/ITO substrates.

Figs. 7a and b and 7e and f, respectively. The NiO NP films had a smooth morphology with a particle size of less than 10 nm, as confirmed using TEM. Moreover, the films of the Cs₂CO₃-intercalated NiO featured a few irregularly shaped particles on their surfaces, due to the non-uniform distribution of Cs₂CO₃, providing a fully packed coverage and, thereby, resulting in a slightly better surface coverage than that of the NiO NPs. The root square mean (RMS) roughness of the NiO + Cs₂CO₃ films (9.05 nm) was less than that of the NiO NPs films (12.9 nm). SEM and AFM images of CH₃NH₃PbI₃ perovskite films on the NiO NP and NiO + Cs₂CO₃ films are provided in **Figs. 7c and d and 7g and h**, respectively. Both films featured large crystals having grains of greater than 1 μm; the RMS roughness was lower in the case of the NiO + Cs₂CO₃ films (32.3 nm) when compared with the bare NiO films (44.3 nm).

PL spectral measurements were performed to examine the quenching of the perovskite by the various charge transporting layers. **Fig. S12 (SI)** presents the steady state PL spectra of glass/perovskite, glass/NiO/perovskite, and glass/NiO + Cs₂CO₃/perovskite. The spectra of the perovskite films in contact with the NiO and NiO + Cs₂CO₃ transport layers were significantly different from that of the reference perovskite film on glass. The NiO + Cs₂CO₃/perovskite films experienced mild quenching, slightly stronger than that of the NiO/perovskite sample, suggesting better charge transfer at NiO + Cs₂CO₃-perovskite interface. PL spectra are typically measured to investigate the quenching phenomena of perovskites at their interfaces with various kinds of contact materials [59]. EIS measurements were performed to examine the interfacial electrical properties of devices A, B, and C. Dark Nyquist plots were drawn using the equivalent circuit model (ECM) [60] for the various device structures (**Figs. S13a and S13b, SI**); the fitting parameters are summarized in **Table S6 (SI)**. The recombination resistances (R_{rec}) and selective contact resistances (R_{sc}) of the devices A–C, obtained by using the fitting parameters of the ECM, as provided in **Fig. S13c (SI)**. Higher values of R_{rec} and R_{sc} were obtained for device B (2.62×10^6 and $2.42 \times 10^5 \Omega \text{ cm}^2$, respectively) than for devices A (1.54×10^3 and $1.49 \times 10^3 \Omega \text{ cm}^2$, respectively) and C (211.3 and 201.3 $\Omega \text{ cm}^2$, respectively), consistent with the improvements in performance of the various device structures. GIWAXS spectra, recorded to determine the changes in the diffraction features of the NiO NP and NiO + 5% Cs₂CO₃ films on silicon substrates, as displayed in **Figs. S14a and S14b (SI)**, respectively. The normalized intensity–radial integration curves (q) of the GIWAXS

patterns of PSCs incorporating NiO and NiO + 5% Cs₂CO₃ are presented in **Figs. S14c and S14d (SI)**, respectively. Both GIWAXS patterns feature the scattering ring at $q_r = 1.45 \text{ \AA}^{-1}$, corresponding to (100) planes [61, 62]. The radial integration curves of the NiO + 5% Cs₂CO₃ and NiO films display full widths at half maximum (FWHMs) for their (100) diffraction peaks of 0.489 and 0.648 [calculated from the areas selected in yellow regions in **Figs. S14c and S14d (SI)**]. The smaller FWHM of the NiO + 5% Cs₂CO₃ film suggested that it had higher crystallinity, larger grains, and bigger the particle size when compared with the NiO film, similar to the conclusions drawn from the SEM and TEM analyses, respectively.

To demonstrate the working mechanism behind the improved performance after intercalating Cs₂CO₃ into NiO films, **Fig. 8a** provides a schematic representation of the accelerated charge extraction through various transport pathways in PSCs having inverted (p–i–n) and conventional planar (n–i–p) structures. For the interface between the Cs₂CO₃-intercalated NiO and the active layer in the inverted structure, holes could be extracted through the highly p-type NiO surface, as indicated by the transport pathways marked by purple arrows. In contrast, for the interface between the Cs₂CO₃-intercalated NiO and the active layer in the planar structure, electrons could be withdrawn efficiently through the doped Cs₂CO₃, as indicated by the transport pathways marked by yellow arrows. To support these working mechanisms, **Fig. 8b–d** displays energy dispersive X-ray spectroscopy (EDS) maps of the Cs₂CO₃-intercalated NiO films, revealing the surface distributions of the Ni, O, and Cs atoms, respectively. **Figs. S15a–c and Table S7 (SI)** presents the scanning TEM image, EDS layered mapping, EDS elemental mapping spectrum, and elemental distribution of intercalated Cs₂CO₃ in NiO films, respectively.

4. Conclusions

In summary, we have prepared ground NiO NPs by high-energy wet-milling grinding method at room temperature. TEM and AFM analysis revealed that average particle size of NiO NPs was 10–20 nm. The Cs₂CO₃-intercalated NiO films display bipolar charge-carrier transporting capabilities for use in inverted and conventional planar PSC device structures. UPS measurements revealed that it was possible to continuously tune the work function, over a range of 1.2 eV, for the Cs₂CO₃-intercalated NiO. Moreover, XPS analysis confirmed the

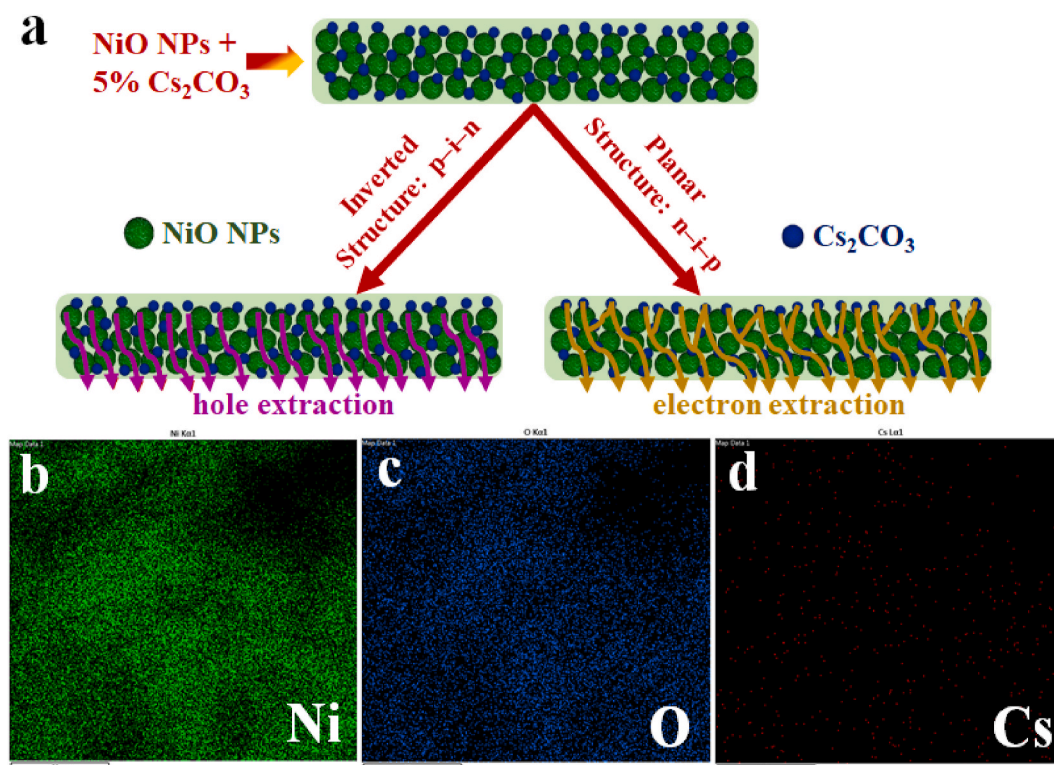


Fig. 8. (a) Schematic representation of accelerated charge extraction in perovskite solar cells having inverted (p-i-n) and planar (n-i-p) structures, from the NiO + 5% Cs₂CO₃ charge transporting layer; purple and yellow arrows indicates the hole and electron transport pathways, respectively. (b-d) EDS mapping of intercalated Cs₂CO₃ in NiO films: (b) Ni, (c) O, and (d) Cs. (For interpretation of the references to color in this figure legend, the reader is referred to the Web version of this article.)

oxidation states and the presence of the Cs₂CO₃ chemical structure. GIWAXS analysis revealed the higher crystallinity and larger grains, for the Cs₂CO₃ doped NiO film. PL spectroscopy revealed the quenching properties of the NiO NPs and the Cs₂CO₃-intercalated NiO films. EIS measurements revealed the interfacial charge properties of the various devices. Three kinds of device structure—devices A, B, and C—displaying high reproducibility provided champion PCEs of 12.08, 13.98, and 9.62%, respectively. Furthermore, inverted PSCs incorporating ground NiO NPs displayed good stability, suggesting the possible importance of such metal oxide charge-carrier transporting layers for PSCs. Indeed, these new low-temperature solution-processed materials displaying bipolar charge-carrier extraction capabilities might also serve as very promising interconnecting layers when applied in flexible tandem solar cells.

CRedit authorship contribution statement

Mriganka Singh: Conceptualization, Methodology, Investigation, Writing - original draft. **Rei-Ting Yang:** Methodology. **Da-Wei Weng:** Methodology. **Hanlin Hu:** Investigation. **Anupriya Singh:** Investigation. **Anisha Mohapatra:** Investigation. **Yu-Ting Chen:** Investigation. **Yu-Jung Lu:** Investigation, Funding acquisition. **Tzung-Fang Guo:** Supervision. **Gang Li:** Supervision. **Hong-Cheu Lin:** Supervision, Funding acquisition. **Chih Wei Chu:** Conceptualization, Writing - review & editing, Project administration, Supervision, Funding acquisition.

Declaration of competing interest

The authors declare that they have no known competing financial interests or personal relationships that could have appeared to influence the work reported in this paper.

Acknowledgements

H.C.L. thanks the Ministry of Science and Technology (MOST) of Taiwan (grant nos. MOST-106-2113-M-009-012-MY3, MOST-107-2221-E-009-043-MY2, and MOST-108-3017-F-009-004) and the Center for Emergent Functional Matter Science of National Chiao Tung University, from the Featured Areas Research Center Program within the framework of the Higher Education of Sprout Project by the Ministry of Education (MOE) in Taiwan, for financial support. Y.J.L. thanks the MOST of Taiwan (grant no. MOST-106-2112-M-001-036-MY3, MOST-109-2112-M-001-043-MY3, and MOST-109-2811-M-001-652) and Academia Sinica (grant no. AS-CDA-108-M08) for financial support. C.W.C. thanks the MOST of Taiwan (grant no. MOST-107-2221-E-001-007-MY3) and Academia Sinica (AS-SS-109-05) for financial support.

Appendix B. Supplementary data

Supplementary data to this article can be found online at <https://doi.org/10.1016/j.solmat.2020.110870>.

Appendix A. Supplementary data

Supplementary data associated with this article can be found in the online version.

References

- [1] X. Zheng, B. Chen, J. Dai, Y. Fang, Y. Bai, Y. Lin, H. Wei, X.C. Zeng, J. Huang, Defect passivation in hybrid perovskite solar cells using quaternary ammonium halide anions and cations, *Nat. Energy* 2 (2017) 17102.
- [2] E.H. Jung, N.J. Jeon, E.Y. Park, C.S. Moon, T.J. Shin, T.-Y. Yang, J.H. Noh, J. Seo, Efficient, stable and scalable perovskite solar cells using poly (3-hexylthiophene), *Nature* 567 (2019) 511–515.

- [3] S.D. Stranks, G.E. Eperon, G. Grancini, C. Menelaou, M.J. Alcocer, T. Leijtens, L. M. Herz, A. Petrozza, H.J. Snaith, Electron-hole diffusion lengths exceeding 1 micrometer in an organometal trihalide perovskite absorber, *Science* 342 (2013) 341–344.
- [4] G. Xing, N. Mathews, S. Sun, S.S. Lim, Y.M. Lam, M. Grätzel, S. Mhaisalkar, T. C. Sum, Long-range balanced electron-and hole-transport lengths in organic-inorganic $\text{CH}_3\text{NH}_3\text{PbI}_3$, *Science* 342 (2013) 344–347.
- [5] A. Kojima, K. Teshima, Y. Shirai, T. Miyasaka, Organometal halide perovskites as visible-light sensitizers for photovoltaic cells, *J. Am. Chem. Soc.* 131 (2009) 6050–6051.
- [6] <https://www.nrel.gov/pv/assets/pdfs/best-research-cell-efficiencies-190416.pdf>.
- [7] Q. Jiang, Y. Zhao, X. Zhang, X. Yang, Y. Chen, Z. Chu, Q. Ye, X. Li, Z. Yin, J. You, Surface passivation of perovskite film for efficient solar cells, *Nat. Photonics* (2019) 1.
- [8] M. Singh, C.-H. Chiang, K.M. Boopathi, C. Hanmandlu, G. Li, C.-G. Wu, H.-C. Lin, C.-W. Chu, A novel ball milling technique for room temperature processing of TiO_2 nanoparticles employed as the electron transport layer in perovskite solar cells and modules, *J. Mater. Chem.* 6 (2018) 7114–7122.
- [9] M. Saliba, T. Matsui, J.-Y. Seo, K. Domanski, J.-P. Correa-Baena, M.K. Nazeeruddin, S.M. Zakeeruddin, W. Tress, A. Abate, A. Hagfeldt, Cesium-containing triple cation perovskite solar cells: improved stability, reproducibility and high efficiency, *Energy Environ. Sci.* 9 (2016) 1989–1997.
- [10] L. Hu, M. Li, K. Yang, Z. Xiong, B. Yang, M. Wang, X. Tang, Z. Zang, X. Liu, B. Li, PEDOT: PSS monolayers to enhance the hole extraction and stability of perovskite solar cells, *J. Mater. Chem.* 6 (2018) 16583–16589.
- [11] J.Y. Jeng, Y.F. Chiang, M.H. Lee, S.R. Peng, T.F. Guo, P. Chen, T.C. Wen, $\text{CH}_3\text{NH}_3\text{PbI}_3$ perovskite/fullerene planar-heterojunction hybrid solar cells, *Adv. Mater.* 25 (2013) 3727–3732.
- [12] Q. Wang, C. Bi, J. Huang, Doped hole transport layer for efficiency enhancement in planar heterojunction organolead trihalide perovskite solar cells, *Nano Energy* 15 (2015) 275–280.
- [13] B. Conings, L. Baeten, C. De Dobbelaere, J. D'Haen, J. Manca, H.G. Boyen, Perovskite-based hybrid solar cells exceeding 10% efficiency with high reproducibility using a thin film sandwich approach, *Adv. Mater.* 26 (2014) 2041–2046.
- [14] G. Yang, H. Tao, P. Qin, W. Ke, G. Fang, Recent progress in electron transport layers for efficient perovskite solar cells, *J. Mater. Chem.* 4 (2016) 3970–3990.
- [15] J. You, Y. Yang, Z. Hong, T.-B. Song, L. Meng, Y. Liu, C. Jiang, H. Zhou, W.-H. Chang, G. Li, Moisture assisted perovskite film growth for high performance solar cells, *Appl. Phys. Lett.* 105 (2014) 183902.
- [16] M. Singh, A. Ng, Z. Ren, H. Hu, H.-C. Lin, C.-W. Chu, G. Li, Facile synthesis of composite tin oxide nanostructures for high-performance planar perovskite solar cells, *Nano Energy* 60 (2019) 275–284.
- [17] U. Kwon, B.-G. Kim, D.C. Nguyen, J.-H. Park, N.Y. Ha, S.-J. Kim, S.H. Ko, S. Lee, D. Lee, H.J. Park, Solution-processible crystalline NiO nanoparticles for high-performance planar perovskite photovoltaic cells, *Sci. Rep.* 6 (2016) 30759.
- [18] R. Azmi, W.T. Hadmojo, S. Sinaga, C.L. Lee, S.C. Yoon, I.H. Jung, S.Y. Jang, High-efficiency low-temperature ZnO based perovskite solar cells based on highly polar, nonwetting self-assembled molecular layers, *Adv. Energy Mater.* 8 (2018) 1701683.
- [19] C. Zuo, L. Ding, Solution-processed Cu_2O and CuO as hole transport materials for efficient perovskite solar cells, *Small* 11 (2015) 5528–5532.
- [20] S. Ye, W. Sun, Y. Li, W. Yan, H. Peng, Z. Bian, Z. Liu, C. Huang, CuSCN -based inverted planar perovskite solar cell with an average PCE of 15.6%, *Nano Lett.* 15 (2015) 3723–3728.
- [21] D.B. Khadka, Y. Shirai, M. Yanagida, K. Miyano, Ammoniated aqueous precursor ink processed copper iodide as hole transport layer for inverted planar perovskite solar cells, *Solar Energy Mater. Sol. Cell.* 210 (2020) 110486.
- [22] W. Sun, S. Ye, H. Rao, Y. Li, Z. Liu, L. Xiao, Z. Chen, Z. Bian, C. Huang, Room-temperature and solution-processed copper iodide as the hole transport layer for inverted planar perovskite solar cells, *Nanoscale* 8 (2016) 15954–15960.
- [23] I. Hwang, K. Yong, Novel CdS hole-blocking layer for photostable perovskite solar cells, *ACS Appl. Mater. Interfaces* 8 (2016) 4226–4232.
- [24] J. Ge, C.R. Grice, Y. Yan, Cu-based quaternary chalcogenide $\text{Cu}_2\text{BaSnS}_4$ thin films acting as hole transport layers in inverted perovskite $\text{CH}_3\text{NH}_3\text{PbI}_3$ solar cells, *J. Mater. Chem.* 5 (2017) 2920–2928.
- [25] J.H. Noh, S.H. Im, J.H. Heo, T.N. Mandal, S.I. Seok, Chemical management for colorful, efficient, and stable inorganic-organic hybrid nanostructured solar cells, *Nano Lett.* 13 (2013) 1764–1769.
- [26] H. Luo, X. Lin, X. Hou, L. Pan, S. Huang, X. Chen, Efficient and air-stable planar perovskite solar cells formed on graphene-oxide-modified PEDOT: PSS hole transport layer, *Nano-Micro Lett.* 9 (2017) 39.
- [27] Z. Zhou, X. Li, M. Cai, F. Xie, Y. Wu, Z. Lan, X. Yang, Y. Qiang, A. Islam, L. Han, Stable inverted planar perovskite solar cells with low-temperature-processed hole-transport bilayer, *Adv. Energy Mater.* 7 (2017) 1700763.
- [28] M. Jørgensen, K. Norrman, F.C. Krebs, Stability/degradation of polymer solar cells, *Solar Energy Mater. Sol. Cell.* 92 (2008) 686–714.
- [29] J. You, L. Meng, T.-B. Song, T.-F. Guo, Y.M. Yang, W.-H. Chang, Z. Hong, H. Chen, H. Zhou, Q. Chen, Improved air stability of perovskite solar cells via solution-processed metal oxide transport layers, *Nat. Nanotechnol.* 11 (2016) 75.
- [30] X. Li, F. Xie, S. Zhang, J. Hou, W.C. Choy, Over 1.1 eV workfunction tuning of cesium intercalated metal oxides for functioning as both electron and hole transport layers in organic optoelectronic devices, *Adv. Funct. Mater.* 24 (2014) 7348–7356.
- [31] X. Li, F. Xie, S. Zhang, J. Hou, W.C. Choy, MoOx and V_2Ox as hole and electron transport layers through functionalized intercalation in normal and inverted organic optoelectronic devices, *Light: Sci. Appl.* 4 (2015) e273.
- [32] M.D. Irwin, D.B. Buchholz, A.W. Hains, R.P. Chang, T.J. Marks, p-Type semiconducting nickel oxide as an efficiency-enhancing anode interfacial layer in polymer bulk-heterojunction solar cells, *Proc. Natl. Acad. Sci. Unit. States Am.* 105 (2008) 2783–2787.
- [33] X.W. Lou, H.C. Zeng, Hydrothermal synthesis of $\alpha\text{-MoO}_3$ nanorods via acidification of ammonium heptamolybdate tetrahydrate, *Chem. Mater.* 14 (2002) 4781–4789.
- [34] M.H. Park, J.H. Li, A. Kumar, G. Li, Y. Yang, Doping of the metal oxide nanostructure and its influence in organic electronics, *Adv. Funct. Mater.* 19 (2009) 1241–1246.
- [35] H.J. Bolink, H. Brine, E. Coronado, M. Sessolo, Phosphorescent hybrid organic-inorganic light-emitting diodes, *Adv. Mater.* 22 (2010) 2198–2201.
- [36] H.-M. Kim, A.R. bin Mohd Yusoff, J.-H. Youn, J. Jang, Inverted quantum-dot light emitting diodes doped aluminum carbonate doped aluminum-zinc-oxide as the cathode buffer layer for high brightness, *J. Mater. Chem. C* 1 (2013) 3924–3930.
- [37] W. Chen, F.Z. Liu, X.Y. Feng, A.B. Djurišić, W.K. Chan, Z.B. He, Cesium doped NiOx as an efficient hole extraction layer for inverted planar perovskite solar cells, *Adv. Energy Mater.* 7 (2017) 1700722.
- [38] X. Yao, J. Qi, W. Xu, X. Jiang, X. Gong, Y. Cao, Cesium-doped vanadium oxide as the hole extraction layer for efficient perovskite solar cells, *ACS Omega* 3 (2018) 1117–1125.
- [39] H. Dong, X. Guo, W. Li, L. Wang, Cesium carbonate as a surface modification material for organic-inorganic hybrid perovskite solar cells with enhanced performance, *RSC Adv.* 4 (2014) 60131–60134.
- [40] J. Liu, S. Shao, G. Fang, B. Meng, Z. Xie, L. Wang, High-efficiency inverted polymer solar cells with transparent and work-function tunable $\text{MoO}_3\text{-Al}$ composite film as cathode buffer layer, *Adv. Mater.* 24 (2012) 2774–2779.
- [41] G. Murdoch, S. Hinds, E. Sargent, S. Tsang, L. Mordoukhovski, Z. Lu, Aluminum doped zinc oxide for organic photovoltaics, *Appl. Phys. Lett.* 94 (2009) 138.
- [42] R. Fernández, J. Estelle, Y. Cesteros, P. Salagre, F. Medina, J.-E. Sueiras, J.-L. G. Fierro, Structural characterization of NiO doped with several caesium loadings, *J. Mol. Catal. Chem.* 119 (1997) 77–85.
- [43] S. Yue, K. Liu, R. Xu, M. Li, M. Azam, K. Ren, J. Liu, Y. Sun, Z. Wang, D. Cao, Efficacious engineering on charge extraction for realizing highly efficient perovskite solar cells, *Energy Environ. Sci.* 10 (2017) 2570–2578.
- [44] J.W. Jung, C.C. Chueh, A.K.Y. Jen, A low-temperature, solution-processable, Cu-doped nickel oxide hole-transporting layer via the combustion method for high-performance thin-film perovskite solar cells, *Adv. Mater.* 27 (2015) 7874–7880.
- [45] S. Sajid, A.M. Elseman, H. Huang, J. Ji, S. Dou, H. Jiang, X. Liu, D. Wei, P. Cui, M. Li, Breakthroughs in NiOx-HTMs towards stable, low-cost and efficient perovskite solar cells, *Nano Energy* 51 (2018) 408–424.
- [46] J.Y. Jeng, K.C. Chen, T.Y. Chiang, P.Y. Lin, T.D. Tsai, Y.C. Chang, T.F. Guo, P. Chen, T.C. Wen, Y.J. Hsu, Nickel oxide electrode interlayer in $\text{CH}_3\text{NH}_3\text{PbI}_3$ perovskite/PCBM planar-heterojunction hybrid solar cells, *Adv. Mater.* 26 (2014) 4107–4113.
- [47] Y.K. Chih, J.C. Wang, R.T. Yang, C.C. Liu, Y.C. Chang, Y.S. Fu, W.C. Lai, P. Chen, T. C. Wen, Y.C. Huang, NiOx Electrode Interlayer and $\text{CH}_3\text{NH}_2/\text{CH}_3\text{NH}_3\text{PbBr}_3$ Interface treatment to markedly advance hybrid perovskite-based light-emitting diodes, *Adv. Mater.* 28 (2016) 8687–8694.
- [48] A. Garcia, G.C. Welch, E.L. Ratcliff, D.S. Ginley, G.C. Bazan, D.C. Olson, Improvement of interfacial contacts for new small-molecule bulk-heterojunction organic photovoltaics, *Adv. Mater.* 24 (2012) 5368–5373.
- [49] D. Bi, C. Yi, J. Luo, J.-D. Décoppet, F. Zhang, S.M. Zakeeruddin, X. Li, A. Hagfeldt, M. Grätzel, Polymer-templated nucleation and crystal growth of perovskite films for solar cells with efficiency greater than 21%, *Nat. Energy* 1 (2016) 16142.
- [50] M. Qin, K. Tse, T.K. Lau, Y. Li, C.J. Su, G. Yang, J. Chen, J. Zhu, U.S. Jeng, G. Li, Manipulating the mixed-perovskite crystallization pathway unveiled by in situ GIWAXS, *Adv. Mater.* 31 (2019) 1901284.
- [51] D.B. Khadka, Y. Shirai, M. Yanagida, K. Miyano, Unraveling the impacts induced by organic and inorganic hole transport layers in inverted halide perovskite solar cells, *ACS Appl. Mater. Interfaces* 11 (2019) 7055–7065.
- [52] S.S. Mali, J.V. Patil, H. Kim, R. Luque, C.K. Hong, Highly efficient thermally stable perovskite solar cells via Cs:NiOx/CuSCN double-inorganic hole extraction layer interface engineering, *Mater. Today* 26 (2019) 8–18.
- [53] S. Rakshit, S. Ghosh, S. Chall, S.S. Mati, S. Moulik, S.C. Bhattacharya, Controlled synthesis of spin glass nickel oxide nanoparticles and evaluation of their potential antimicrobial activity: a cost effective and eco friendly approach, *RSC Adv.* 3 (2013) 19348–19356.
- [54] Y.-C. Jeong, J. Nam, J. Kim, C.S. Kim, S. Jo, Enhancing thermal oxidation stability of silver nanowire transparent electrodes by using a cesium carbonate-incorporated overcoating layer, *Materials* 12 (2019) 1140.
- [55] J.-H. Huang, H.-Y. Wei, K.-C. Huang, C.-L. Chen, R.-R. Wang, F.-C. Chen, K.-C. Ho, C.-W. Chu, Using a low temperature crystallization process to prepare anatase TiO_2 buffer layers for air-stable inverted polymer solar cells, *Energy Environ. Sci.* 3 (2010) 654–658.
- [56] S. Nho, G. Baek, S. Park, B.R. Lee, M.J. Cha, D.C. Lim, J.H. Seo, S.-H. Oh, M. H. Song, S. Cho, Highly efficient inverted bulk-heterojunction solar cells with a gradiently-doped ZnO layer, *Energy Environ. Sci.* 9 (2016) 240–246.
- [57] H.-B. Kim, H. Choi, J. Jeong, S. Kim, B. Walker, S. Song, J.Y. Kim, Mixed solvents for the optimization of morphology in solution-processed, inverted-type perovskite/fullerene hybrid solar cells, *Nanoscale* 6 (2014) 6679–6683.
- [58] P. Cui, D. Wei, J. Ji, H. Huang, E. Jia, S. Dou, T. Wang, W. Wang, M. Li, Planar p-n homojunction perovskite solar cells with efficiency exceeding 21.3%, *Nat. Energy* 4 (2019) 150–159.

- [59] K.-C. Wang, J.-Y. Jeng, P.-S. Shen, Y.-C. Chang, E.W.-G. Diau, C.-H. Tsai, T.-Y. Chao, H.-C. Hsu, P.-Y. Lin, P. Chen, P-type mesoscopic nickel oxide/organometallic perovskite heterojunction solar cells, *Sci. Rep.* 4 (2014) 4756.
- [60] Q. Shen, A. Ng, Z. Ren, H.C. Gokkaya, A.B. Djurišić, J.A. Zapien, C. Surya, Characterization of low-frequency excess noise in $\text{CH}_3\text{NH}_3\text{PbI}_3$ -based solar cells grown by solution and hybrid chemical vapor deposition techniques, *ACS Appl. Mater. Interfaces* 10 (2017) 371–380.
- [61] M.-H. Jao, C.-C. Cheng, C.-F. Lu, K.-C. Hsiao, W.-F. Su, Low temperature and rapid formation of high quality metal oxide thin film via a hydroxide-assisted energy conservation strategy, *J. Mater. Chem. C* 6 (2018) 9941–9949.
- [62] M. Banerjee, S. Mukherjee, S. Maitra, Synthesis and characterization of nickel oxide doped barium strontium titanate ceramics, *Cerâmica* 58 (2012) 99–104.